CrystEngComm

PAPER

Single-crystalline mesoporous ZnO nanosheets prepared with a green antisolvent method exhibiting excellent photocatalytic efficiencies

Ji-Yao Dong,[a] Cheng-Hsien Lin,[a] Yung-Jung Hsu,[b] Shih-Yuan Lu*[a] and David Shan-Hill Wong*[a]

Single-crystalline mesoporous ZnO nanosheets were prepared with a green, deep eutectic solvent based antisolvent process followed by calcination at 300 °C. The antisolvent procedure led to formation of nanosheets of a mixed composition of zinc carbonate hydroxide and ZnO, calcination of which generated the product. The product nanosheets were ultrathin with a thickness of around 10 nm and pore sizes increasing from less than 10 nm to several tens nanometers with increasing calcination time and temperature. These nanosheets exhibited excellent photocatalytic efficiencies as good as that of a commercial photocatalyst, P-25 TiO_2 in terms of photocatalytic degradation of a model pollutant, methylene blue. The success is attributable to the structural advantages of the nanosheets of being ultrathin, mesoporous, and single-crystalline.

Introduction

Two-dimensional (2-D) nanomaterials, including nanosheets[1–5] and nanoplates,[6–8] receive much less research attention than 0-D (nanoparticles and quantum dots) and 1-D (nanorods, nanowires, nanotubes, *etc.*) materials. The unique structural features of 2-D nanomaterials, such as ultrathin thicknesses and possibly exposed specific crystalline planes, however may prove advantageous for a wide range of charge transport involved and surface interaction/reaction oriented applications, such as electrodes of dye-sensitized solar cells,[1,9,10] gas sensors,[11,12] supercapacitors, lithium ion batteries, photocatalytic water splitting, photocatalysis,[13] *etc.*

Single-crystalline, mesoporous nanosheets possess further structural advantages of high specific surface areas and the absence of grain boundaries. The former provides a large amount of active sites for surface interactions/reactions to take place, while the latter enables rapid charge transport, essential for many surface interaction/reaction oriented applications. Nevertheless, the study of single-crystalline, mesoporous nanosheets has been quite limited.[10,14,15] The synthesis of single-crystalline, mesoporous nanosheets takes two steps, with precursor nanosheets of layered crystallographic structure produced in the first step and pores and single-crystallinity of the product nanosheets developed in the second step through a calcination triggered topotactic reaction. The precursor nanosheets belong to the class of layered hydroxide salts (LHS) or layered double hydroxides (LDH), both possessing crystallographic structure built from the stacking of two-dimensional units.[16] These LHS or LDH may be transformed into corresponding oxides while retaining the characteristic layered structure, upon thermal decomposition.[16–18] The precursor nanosheets are produced by hydrothermal[10,14] or solvothermal[15] processes, often requiring long reaction times and use of surfactants.

In this article, we report a brand new way of creating single-crystalline, mesoporous nanosheets. It is a deep eutectic solvent (DES) based antisolvent process followed by calcination at 300 °C. Deep eutectic solvents are a new class of room temperature ionic liquids, which possess many advantageous solvent characteristics including high polarities, high ionic conductivities, negligible vapour pressures, good thermal stabilities, and wide liquid windows, and thus are considered a new class of green solvents to replace commonly and largely used and often hazardous organic solvents in many applications.[19] Deep eutectic solvents can be prepared by simply mixing quaternary ammonium salts with hydrogen-bond donors at temperatures often lower than 100 °C. A wide variety of DES may be prepared since there is a large selection of quaternary ammonium salts and many hydrogen-bond donors are available including amides, acids, alcohols, and amines.[20] These DES are good solvents for metal oxides and highly soluble in common solvents such as water, in which metal oxides are not soluble.[20] The solvent property of the DES toward a metal oxide will be lost when the solution is mixed with an antisolvent that shows no solvation ability toward the metal oxide, thus leading to generation of various nanostructures of the metal oxide. The resulting nanostructures may be tuned by adjusting the way of mixing and/or addition of structure-directing reagents.[21,22]

As illustrated in Fig. 1, the preparation of single-crystalline, mesoporous ZnO nanosheets with the present antisolvent based

[a]Department of Chemical Engineering, National Tsing-Hua University, Hsinchu, 30013, Taiwan, Republic of China. E-mail: sylu@mx.nthu.edu.tw; dshwong@che.nthu.edu.tw; Fax: +886 3-5715408; Tel: +886 3-5714364
[b]Department of Materials Science and Engineering, National Chiao-Tung University, Hsinchu, 30010, Taiwan, Republic of China
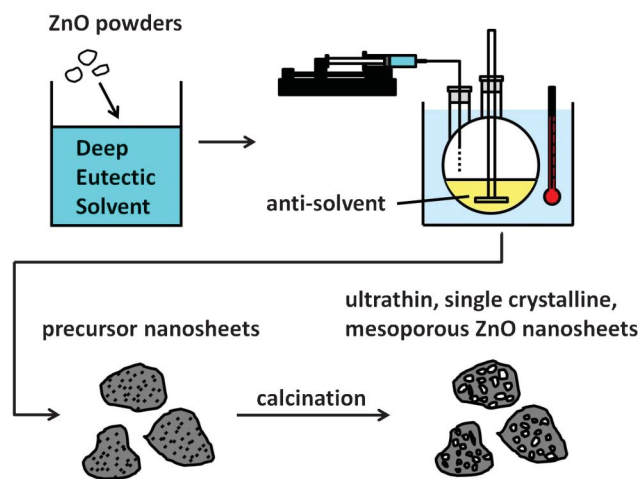
Fig. 1 Illustration of preparation procedures of single-crystalline, mesoporous ZnO nanosheets with the present antisolvent based process.

process involves only simple operations of powder dissolution, solution mixing, and calcination, without use of special equipment. When the ZnO-containing DES solution is mixed with the antisolvent, the antisolvent, a non-solvent toward ZnO but good solvent for the DES, dissolves the DES and thus forces the ZnO precursor to precipitate out, forming the precursor nanosheets, calcination of which leads to the formation of the product porous nanosheets.

In this article, precursor nanosheets of ZnO were prepared from the antisolvent process by using a deep eutectic solvent, formed by urea and choline chloride (UCC), as the solvent and de-ionized water as the antisolvent. Both constituents of UCC are cheap and commonly found in bio-organisms and are therefore environmentally benign. Product nanosheets were produced by calcination of the precursor nanosheets at 300 °C for a short period of time. These nanosheets were single-crystalline, ultrathin, and mesoporous with a high specific surface area, and demonstrated their excellent photocatalytic efficiency toward methylene blue degradation, as good as that of a commercial photocatalyst, P-25 TiO_2 powder, which is rarely if not never achieved by pristine ZnO.

Experimental methods

Preparation of mesoporous ZnO nanosheets

All chemicals were used without further purification. An amount of 150 g of UCC was first prepared by mixing 69 g of urea (Riedel-de Haën, 99.5%) and 81 g of choline chloride (Sigma-Aldrich, 98%), at a molar ratio of 2 to 1, in a glove box of an argon atmosphere. An amount of 3.6 g of ZnO powder (Sigma-Aldrich, 99%) was then added to the UCC to afford a solution containing roughly 24 000 ppm of ZnO. These UCC solutions were kept in an oven at 70 °C for several days until all ZnO powder dissolved and clear solutions were obtained. Ten grams of ZnO-containing UCC solution were injected into 200 mL de-ionized water, the antisolvent, at 70 °C at a rate of 2 g h^{-1}. A white suspension was obtained and the precipitate was collected and washed with water and ethanol to remove remaining UCC and impurities. The precipitate was then calcined at 300 or 400 °C for 30 min or 5 h to afford the product nanosheets.

Photocatalytic performance measurement

The photocatalytic performance of the mesoporous ZnO nanosheets was evaluated by the photodegradation of methylene blue (MB) under UV illumination. All photocatalysis experiments were conducted at room temperature. In a typical run, 4.0 mg of photocatalyst were added into 20 mL of MB solution (1×10^{-5} M). Prior to irradiation, the suspension was stirred in the dark for 60 min to reach the adsorption equilibrium between the MB and photocatalyst. At certain time intervals of irradiation, samples were analyzed with a UV-visible spectrophotometer to determine the concentration variation of MB through recording the corresponding absorbance of the characteristic peak of 665 nm. For the photocatalytic degradation measurements of rhodamine B (RhB), 10 mg of photocatalyst were used and the absorbance of the characteristic peak of 554 nm was measured for the RhB concentration determination.

Measurement of hydroxyl radicals

Hydroxyl radicals produced during the photocatalytic reaction are considered the major active species responsible for the photocatalytic degradation of pollutant molecules.[23,24] Yu and co-workers have developed a photoluminescence-based (PL) technique for the quantification of the hydroxyl radicals.[25–27] Here, we followed their procedures to investigate the correlation between the photocatalytic performance of the photocatalyst and the relative hydroxyl radical concentration measured with the PL technique. Briefly, 10 mg of photocatalyst were dispersed in 20 mL of 10^{-3} M coumarin (COU) aqueous solution. At UV irradiations, COU, a poorly fluorescent molecule, reacts with the hydroxyl radicals produced from the photocatalyst to form the highly fluorescent 7-hydroxycoumarin (7HC) molecule, whose concentration is then determined with the PL intensity (Hitachi, F-4500) recorded at 456 nm with an excitation wavelength of 332 nm. A convenient OH-index was defined by Yu and co-workers[25] as the formation rate of the hydroxyl radicals of the photocatalyst normalized with that of the P-25 TiO_2 to quantify the relative photocatalytic capability of the photocatalyst. We correlated this index with the photocatalytic performances of the present mesoporous ZnO nanosheets in terms of photocatalytic degradation of MB and RhB.

Characterizations

The morphology and dimensions of the products were examined with a field-emission scanning electron microscope (FESEM, Jeol, JSM-6500F). The crystallographic structure of the samples was investigated with an X-ray diffractometer (XRD, MAC Science, MXP18) and a high-resolution transmission electron microscope (HRTEM, JEOL, JEM-2100) operated at 200 kV. Brunauer–Emmett–Teller (BET) specific surface areas and Barret–Joyner–Halenda (BJH) pore volumes of the samples were determined from the N_2 adsorption/desorption isotherms. UV-visible spectra were collected with a Hitachi U-3900H at room temperature under ambient atmosphere.

Results and discussion

The as-prepared product from the antisolvent process was nanosheets randomly stacked together as shown in Fig. 2(a).
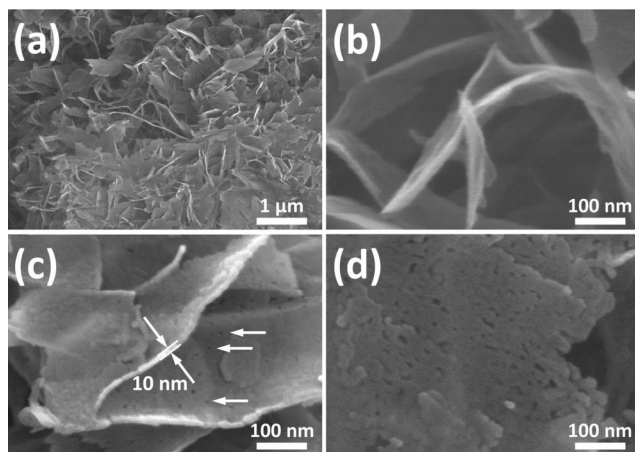
Fig. 2 SEM images of as-prepared samples at a (a) low and (b) high magnification, and samples prepared by calcination at 300 °C for (c) 30 min and (d) 5 h.

These nanosheets were of a size of several hundred nanometers and without the evident presence of pores as judged from a higher magnification SEM image shown in Fig. 2(b). Pores however clearly emerged upon heat treatment at 300 °C. After a calcination time of 30 min, tiny pores with a size less than 10 nm formed in the nanosheets as indicated by arrows in Fig. 2(c). The thickness of these mesoporous nanosheets was around 10 nm. The number and size of the pores increased with increasing the calcination time to 5 h. As shown in Fig. 2(d), pores with a size larger than 20 nm can be readily found. If the calcination temperature was raised to 400 °C, the pores grew even larger (SEM image not shown).

The XRD patterns of the as-prepared product and products calcined at 300 °C for 30 min and 5 h are presented in Fig. 3. The as-prepared product was composed of a mixed composition of zinc oxide (hexagonal wurtzite, JCPDS # 36-1451) and a zinc carbonate hydroxide (ZCH), $Zn_4CO_3(OH)_6 \cdot H_2O$ (JCPDS # 11-0287). The ZCH was produced from the reaction of urea and Zn^{2+} during the antisolvent process. The hydrolysis of urea
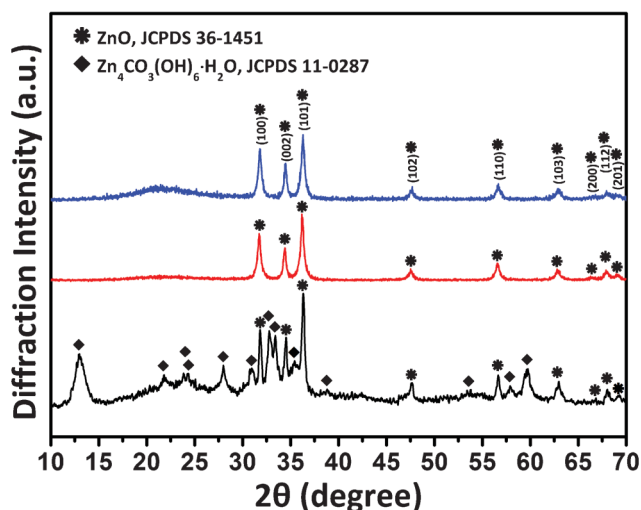
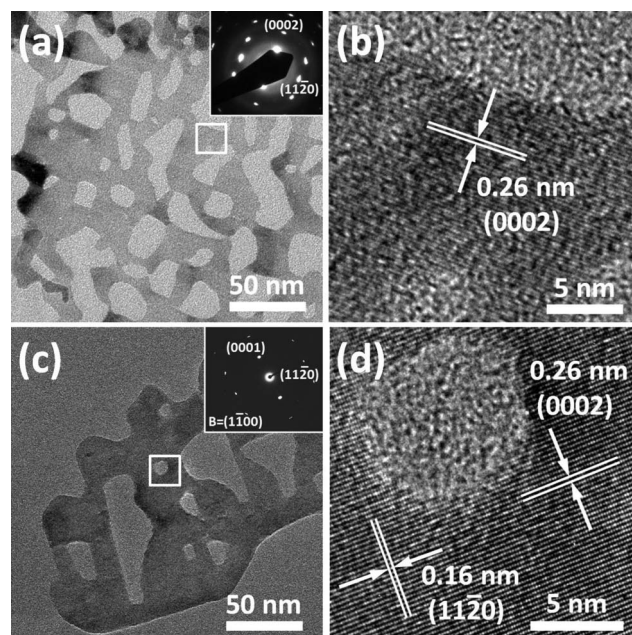provided the carbonate and hydroxide ions necessary to form the ZCH with Zn^{2+}.[16,28] Here, urea served not only as the hydrogen-bond donor to form the deep eutectic solvent with choline chloride for the dissolution of the ZnO powders, but also as the carbonate and hydroxide ion sources to form the ZnO precursor, ZCH, with Zn^{2+}. The ZCH is an LHS and possesses an inherent 2D crystallographic structure.[16] The calcination of the ZCH released CO_2 and H_2O to create voids and initiate crystallographic restructuring of the nanosheets through a topotactic reaction, retaining the 2D morphology after the thermal decomposition as evident from Fig. 2.[16] The aggregation of these voids, thermodynamically favourable to reduce the total surface area of the newly created solid–gas interfaces, formed pores in the nanosheets. Surprisingly, in addition to the ZCH, crystalline ZnO was also formed in the as-prepared sample, in contrast to previously reported results on the preparation of LHS, in which only LHS were produced.

Upon thermal treatment at 300 °C for a short period of time, 30 min, the ZCH decomposed to form ZnO of good crystallinity, as judged from the well-defined diffraction peaks of the XRD pattern. Increasing the thermal treatment time to 5 h did not give appreciable differences in terms of the crystalline quality of the product. The number and size of the resulting pores however increased as noted in Fig. 2(d).

The crystallinity and pore structure of the products were further studied with TEM and HRTEM images and corresponding SAED patterns, as shown in Fig. 4. Fig. 4(a) shows the TEM image and SAED pattern for products obtained from calcination at 300 °C for 5 h. The irregularly shaped pores are randomly distributed on the nanosheet with pore sizes ranging from 5 to 50 nm. The dotted SAED pattern indicated the single-crystallinity of the porous nanosheet. The dots however were stretched, implying the presence of structural defects of non-negligible

Fig. 3 XRD patterns of as-prepared sample and samples prepared by calcination at 300 °C for 30 min and 5 h (from bottom to top).

Fig. 4 (a) TEM and (b) HRTEM images taken from the sample prepared by calcination at 300 °C for 5 h, and (c) TEM and (d) HRTEM images taken from the sample prepared by calcination at 400 °C for 2 h.

amounts. The crystalline planes (0002) and (11$\bar{2}$0) of wurtzite ZnO can be identified from the SAED pattern. Fig. 4(b) is an HRTEM image of the labelled area of Fig. 4(a). An interlayer spacing of 0.26 nm was determined, in good agreement with the *d*-spacing of the (0002) planes of wurtzite ZnO. Several other HRTEM images were taken from different locations of Fig. 4(a) (data not shown) and showed the same crystalline plane orientation as that of Fig. 4(b), a further confirmation of the single-crystallinity of the whole porous sheet. It is interesting to note that the exposed crystalline planes of the present porous ZnO nanosheets, obtained from the topotactic transformation of the corresponding LHS,[1,10,14] are different from those of non-porous ZnO nanosheets, produced from retarded *c*-plane growth.[29,30]

Fig. 4(c) and (d) present the same set of information for products obtained from calcination at 400 °C for 2 h. The increase in calcination temperature to 400 °C did improve the single-crystallinity of the porous nanosheets, as judged from the more well-defined dot pattern of SAED and the much better resolved lattice fringes of the HRTEM image. In fact, the lattice fringes remain well-resolved even around the pore edge. In addition to the interlayer spacing along the (0002) direction, that along the direction normal to (0002) can also be determined to be 0.16 nm, again in good agreement with the *d*-spacing of the (11$\bar{2}$0) planes of wurtzite ZnO. It is evident that the nanosheets produced by the present process are mesoporous, single-crystal-line wurtzite ZnO.

The microstructure of the nanosheets was further characterized with the N_2 adsorption/desorption isotherms. Fig. 5(a) and (b) show the N_2 adsorption/desorption isotherms and the corresponding pore size distribution curves of the as-prepared sample and the product obtained with calcination at 300 °C for 5 h. Both samples exhibited a type IV isotherm of a type H3 hysteresis loop, typical of mesoporous materials. The BET specific surface areas were determined to be 92 and 90 m^2 g^{-1} for the as-prepared and calcined samples, respectively, with not much difference resulting from the calcination. The pore size distributions however revealed some interesting phenomena. The one obtained from the as-prepared sample showed a bi-modal size distribution, with the smaller sizes peaking at 5.1 nm and the larger sizes at 23 nm. The smaller pore sizes were contributed by the pores of the nanosheets, whereas the larger ones came from the stacking of the nanosheets.[26] These small pores of the as-prepared nanosheets were not evidently visible from the SEM image presented in Fig. 2(b) probably because of the spatial resolution limit and improper sampling view angles. These small pores aggregated to form larger pores upon thermal treatment, which was thermodynamically favourable for reduction of the total energy through diminishing higher energy solid–gas interfaces. As a result, the pores of the nanosheets grew larger to acquire pore sizes comparable to those formed through nanosheet stacking, leading to the change in pore size distribution shape from bi-modal for the as-prepared sample to single-modal for the calcined sample.

It is worth mentioning that the present products possessed higher specific surface areas and smaller nanosheet thicknesses than products from both microwave-assisted[1] and hydrothermal processes.[10,14] The specific surface area of the product prepared by calcination at 300 °C for 30 min, 91 m^2 g^{-1}, was about the
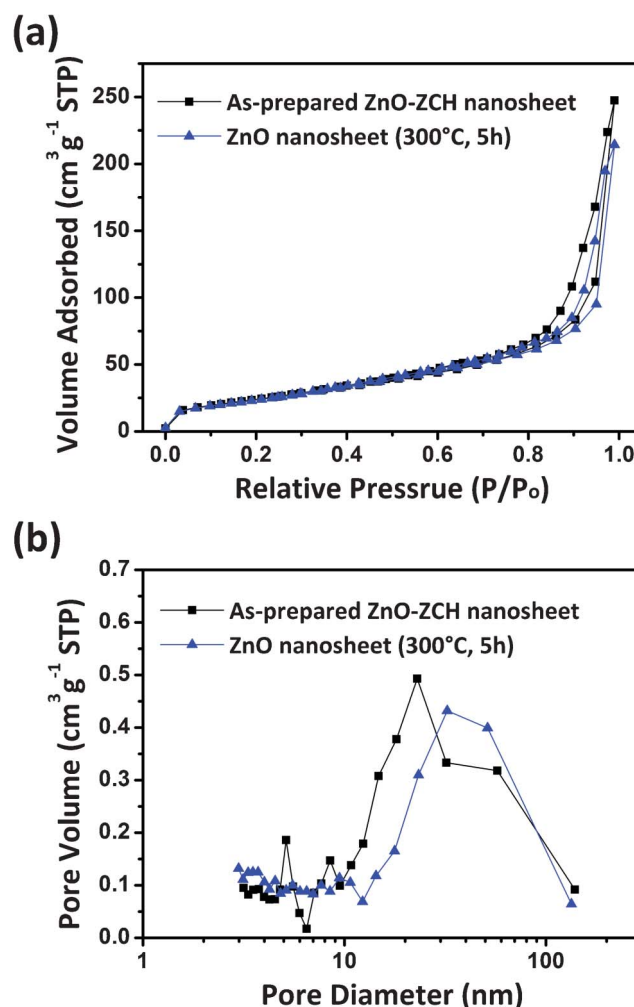

Fig. 5 (a) N_2 adsorption/desorption isotherms and (b) pore size distributions for the as-prepared sample and sample prepared by calcination at 300 °C for 5 h.

same with that of the product prepared by calcination at 300 °C for 5 h. The specific surface area however drastically decreased to 40 m^2 g^{-1} at a higher calcination temperature of 400 °C for 2 h.

From the above characterizations, the ZnO nanosheets produced from the present process possessed mesoporosity, single-crystallinity, high surface areas, and ultrathin thicknesses. These characteristics are beneficial for photocatalytic applications. Here, we demonstrated their outstanding photocatalytic performances toward the photodegradation of methylene blue and rhodamine B, taking the commercial photocatalyst, P-25 TiO$_2$, as the comparison basis. Fig. 6(a) and (b) show the normalized model pollutant (MB in Fig. 6(a) and RhB in Fig. 6(b)) concentration *vs.* irradiation time curves for four samples, including the as-prepared ZCH/ZnO nanosheet, porous nanosheets obtained with calcination at 300 °C for 30 min and 5 h, and P-25 TiO$_2$. Also included for comparison are the curves obtained from irradiation in the absence of the photocatalyst. For the photocatalytic degradation of MB, evidently, the as-prepared sample exhibited the worst photocatalytic performance, almost the same with that of the no-catalyst case,
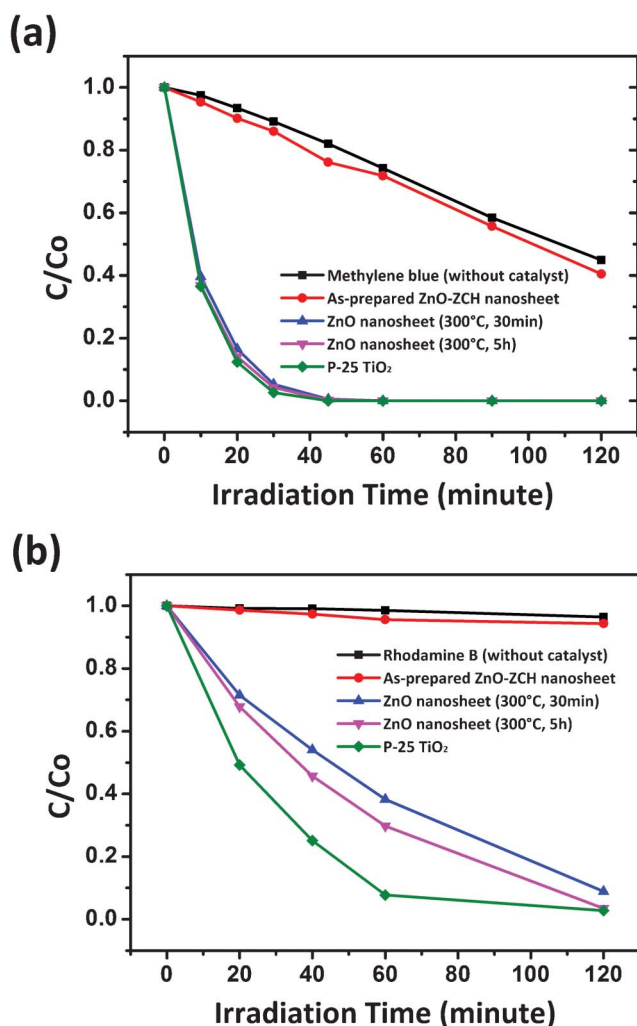
(a)

(b)

Fig. 6 Normalized concentration decay curves *vs.* irradiation time for as-prepared sample, samples prepared by calcination at 300 °C for 30 min and 5 h, and P-25 TiO$_2$. (a) Methylene blue and (b) rhodamine B.

whereas the other three samples showed almost the same level of photocatalytic efficiency, with the P-25 TiO$_2$ being the best followed by the 5 h calcination sample and then 30 min calcination sample. As judged from the XRD pattern, the as-prepared sample contained a good portion of ZCH, which was not photocatalytically active. The existence of the ZCH may also serve as charge carrier traps to impede the electron–hole separation necessary for the photocatalytic functionality.

Surprisingly, the two calcined nanosheet samples exhibited almost the same level of photocatalytic efficiency as P-25 TiO$_2$, with the longer calcination time sample, 5h, being slightly better than the shorter calcination time sample, 30 min. Several factors may have contributed to this success. First, these nanosheets were ultrathin and single-crystalline, so that the migration of the photo-induced holes to the nanosheet surface to trigger the oxidation of the adsorbed methylene blue molecules can be rapidly accomplished because of the short travel distance and absence of grain boundaries to impede charge transport or to trap the holes. Second, the high specific surface area of the mesoporous nanosheets, about twice of that of P-25 TiO$_2$ (47.5 m^2 g^{-1}), provided abundant active sites for the photocatalytic

degradation to take place. Third, it has been demonstrated that the *c*-plane of ZnO is a superior facet in photocatalytic activity.[31] Although the exposed planes of the nanosheet surfaces were not the *c*-plane, the side walls of the pores did contain the *c*-plane. The abundant pores distributed uniformly throughout the whole nanosheets thus offered a good portion of exposed *c*-planes for the effective photocatalytic reactions.

We further examined the photocatalytic performances of the four photocatalysts with respect to the degradation of rhodamine B, a model pollutant more resistant to photocatalytic reactions.[32,33] As evident from Fig. 6(b), it took a much longer time to degrade RhB. Again, the as-prepared sample showed the worst performance, almost the same with that of the no-catalyst case. The differences in photocatalytic capability between the other three photocatalysts enlarged under this more severe test condition. The P-25 TiO$_2$ performed the best, with the 5 h calcination sample coming second and the 30 min calcination sample last. The OH-indices of the three photocatalysts were measured with the PL-based technique,[25–27] taking that of the P-25 TiO$_2$ as the normalization basis. The results were 100, 30.2, and 28.6 for the P-25 TiO$_2$, 5 h calcination sample, and 30 min calcination sample, respectively, correlating well with the order of the photocatalytic performance among the three photocatalysts.

The re-usability of the present photocatalyst was also investigated. The amount of RhB degraded at the end of a 2 h irradiation session *versus* the initial RhB amount was measured for three consecutive sessions for the 30 min calcination sample. We took the datum of the first session as a normalization basis for comparison purposes, and the results were 1.00, 1.03, and 1.01 for the three consecutive sessions, showing an excellent re-usability of the present photocatalyst. The good stability of ZnO towards possible photo-corrosion in neutral solution of RhB has been demonstrated by Yu and Yu with ZnO hollow spheres.[34]

Conclusions

In conclusion, we have developed a green, deep eutectic solvent based antisolvent process for production of ZCH nanosheets, calcination of which at 300 °C for a short time period led to formation of ultrathin, single-crystalline, mesoporous ZnO nanosheets. The product nanosheets exhibited outstanding photocatalytic properties, as good as those of a commercial photocatalyst, P-25 TiO$_2$, attributable to their structural advantages of being ultrathin, mesoporous, and single-crystalline.

Acknowledgements

References

1 Z. H. Jing and J. H. Zhan, *Adv. Mater.*, 2008, **20**, 4547.
2 S. H. Yu and M. Yoshimura, *Adv. Mater.*, 2002, **14**, 296.
3 X.-S. Fanf, C.-H. Ye, L.-D. Zhang, Y.-H. Wang and Y.-C. Wu, *Adv. Funct. Mater.*, 2005, **15**, 63.
4 J.-H. Park, H.-J. Choi, Y.-J. Choi, S.-H. Sohn and J.-G. Park, *J. Mater. Chem.*, 2004, **14**, 35.

5 X. S. Fang, C. H. Ye, X. S. Peng, Y. H. Wang, Y. C. Wu and L. D. Zhang, *J. Mater. Chem.*, 2003, **13**, 3040.

6 R. C. Jin, Y. C. Cao, E. C. Hao, G. S. Metraux, G. C. Schatz and C. A. Mirkin, *Nature*, 2003, **425**, 487.

7 Y. J. Xiong, J. M. McLellan, J. Y. Chen, Y. D. Yin, Z. Y. Li and Y. N. Xia, *J. Am. Chem. Soc.*, 2005, **127**, 17118.

8 K. H. Park, K. Jang and S. U. Son, *Angew. Chem., Int. Ed.*, 2006, **45**, 4608.

9 E. Hosono, S. Fujihara, I. Honna and H. S. Zhou, *Adv. Mater.*, 2005, **17**, 2091.

10 Y. C. Qiu, W. Chen and S. H. Yang, *J. Mater. Chem.*, 2010, **20**, 1001.

11 J. Zhang, S. R. Wang, M. J. Xu, Y. Wang, B. L. Zhu, S. M. Zhang, W. P. Huang and S. H. Wu, *Cryst. Growth Des.*, 2009, **9**, 3532.

12 J. Liu, Z. Guo, F. Meng, T. Luo, M. Li and J. Liu, *Nanotechnology*, 2009, **20**, 125501.

13 L. Wang, Y. Zheng, X. Li, W. Dong, W. Tang, B. Chen, C. Li, X. Li, T. Zhang and W. Xu, *Thin Solid Films*, 2011, **519**, 5673.

14 X. F. Zhou, Z. L. Hu, Y. Q. Fan, S. Chen, W. P. Ding and N. P. Xu, *J. Phys. Chem. C*, 2008, **112**, 11722.

15 J. C. Hu, K. K. Zhu, L. F. Chen, H. J. Yang, Z. Li, A. Suchopar and R. Richards, *Adv. Mater.*, 2008, **20**, 267.

16 G. G. C. Arizaga, K.G. Satyanarayana and F. Wypych, *Solid State Ionics*, 2007, **178**, 1143.

17 L. Markov, R. Ioncheva, M. Marinov and K. Ivanov, *Mater. Chem. Phys.*, 1990, **26**, 493.

18 L. Markov, K. Petrov and A. Lyubchova, *Solid State Ionics*, 1990, **39**, 187.

19 R. D. Rogers and K. R. Seddon, *Ionic Liquids III: Fundamentals, Progress, Challenges, and Opportunities*, American Chemical Society, Washington DC, 2005.

20 A. P. Abbott, P. M. Cullis, M. J. Gibson, R. C. Harris and E. Raven, *Green Chem.*, 2009, **9**, 868.

21 J.-Y. Dong, Y.-J. Hsu, D. S.-H. Wong and S.-Y. Lu, *J. Phys. Chem. C*, 2010, **114**, 8867.

22 J.-Y. Dong, W.-H. Lin, Y.-J. Hsu, D. S.-H. Wong and S.-Y. Lu, *CrystEngComm*, 2011, **13**, 6218.

23 K. Ishibashi, A. Fujishima, T. Watanabe and K. Hashimoto, *Electrochem. Commun.*, 2000, **2**, 207.

24 K. Ishibashi, A. Fujishima, T. Watanabe and K. Hashimoto, *J. Photochem. Photobiol., A*, 2000, **134**, 139.

25 Q. Xiang, J. Yu and P. K. Wong, *J. Colloid Interface Sci.*, 2011, **357**, 163.

26 J. Yu, Q. Xiang, J. Rana and S. Mann, *CrystEngComm*, 2010, **12**, 872.

27 S. Liu, C. Li, J. Yu and Q. Xiang, *CrystEngComm*, 2011, **13**, 2533.

28 X. B. Wang, W. P. Cai, Y. X. Lin, G. Z. Wang and C. H. Liang, *J. Mater. Chem.*, 2010, **20**, 8582.

29 A. Mclaren, T. Valdes-Solis, G. Li and S. C. Tsang, *J. Am. Chem. Soc.*, 2009, **131**, 12540.

30 X.-G. Han, H.-Z. He, Q. Kuang, X. Zhou, X.-H. Zhang, T. Xu, Z.-X. Xie and L.-S. Zheng, *J. Phys. Chem. C*, 2009, **113**, 584.

31 A. McLaren, T. Valdes-Solis, G. Q. Li and S. C. Tsang, *J. Am. Chem. Soc.*, 2009, **131**, 12540.

32 Y. Guo, X. Yang, F. Ma, K. Li, L. Xu, X. Yuan and Y. Guo, *Appl. Surf. Sci.*, 2010, **256**, 2215.

33 W. Yao, B. Zhang, C. Huang, C. Ma, X. Songa and Q. Xu, *J. Mater. Chem.*, 2012, **22**, 4050.

34 J. Yu and X. Yu, *Environ. Sci. Technol.*, 2008, **42**, 4902.